RESEARCH ARTICLE

ADVANCED FUNCTIONAL MATERIALS
www.afm-journal.de

Highly-Soft, Scalable, Personalizable Skin-Interfaced Systems via Self-Healing Gels

Anran Zhang, Zhang Yue, Bryant Grove, Yizhang Wu, Yihan Liu, Yuxin Su, Yu Chen, Elvis Tanyi, Sicheng Xing, Brayden Davis, Kihyun Lee, Gongkai Yuan, Wanrong Xie, Yihang Wang, Zhibo Zhang, Arjun Putcha, Kate Huang, Haozhe Wang, Boran Ma, Ke Cheng,* and Wubin Bai**

Precision healthcare relies upon ubiquitous biofeedback to optimize therapy individually for nuanced and dynamic needs. However, grand challenges reside in the lack of soft, highly personalizable monitors that are scalable in manufacturing and reversibly interchangeable upon the evolution of needs. Herein, a customizable soft wearable platform is presented that can seamlessly integrate diverse functional modules, including physical and biochemical sensors, stimulators, and energy storage devices, tailored to various health monitoring scenarios, while can self-repair after certain mechanical damage. The platform supports versatile physiological sensing and therapeutic intervention due to its compatibility with wide-ranging functional nanomaterials. A bilayer microporous foam embedded in the gel improves sweat management for comfortable and reliable on-body biomarker monitoring. Furthermore, flexible self-healing zinc-air batteries using ion gel electrolytes provide opportunities for self-powered, closed-loop systems. On-body demonstrations validate the platform's capability to monitor physiological and metabolic states under real-world conditions. This work provides a scalable and adaptable materials-based solution for real-time personalized health monitoring, advancing wearable bioelectronics to meet evolving healthcare demands.

1. Introduction

Precision medicine has gained significant attention due to its potential to provide tailored healthcare solutions that address individual needs.[1,2] Wearable systems, as essential elements for precision medicine, however, often suffer from viable leverage between soft mechanics and personalizable form factors. Unlike multifunctional platforms that integrate a wide range of sensors and actuators, personalized systems allow for customized selection of specific functionalities, which can reduce device form factors, enhance functional relevance, and improve system efficiency with just-in-time manufacturing compatibility, similar to that in the automotive industry, where various components are assembled on-demand to meet unique customer specifications. Personalized wearable devices, due to their flexibility, specificity, and non-invasiveness, can conveniently monitor the most relevant set of physiological parameters for each

A. Zhang, Y. Wu, Y. Liu, K. Lee, W. Xie, Y. Wang, A. Putcha, W. Bai
Department of Applied Physical Sciences
University of North Carolina at Chapel Hill
Chapel Hill, NC 27599, USA
E-mail: wbai@unc.edu

Z. Yue, K. Cheng
Department of Biomedical Engineering
Columbia University
New York, NY 10027, USA
E-mail: ke.cheng@columbia.edu

B. Grove, B. Ma
School of Polymer Science and Engineering
University of Southern Mississippi
Hattiesburg, MS 39406, USA
E-mail: boran.ma@usm.edu

The ORCID identification number(s) for the author(s) of this article can be found under https://doi.org/10.1002/adfm.202507821

Y. Su
Department of Physics and Astronomy
University of North Carolina at Chapel Hill
Chapel Hill, NC 27599, USA

Y. Chen
Department of Statistics and Operations Research
University of North Carolina at Chapel Hill
Chapel Hill, NC 27599, USA

E. Tanyi, S. Xing, B. Davis, G. Yuan
UNC/NCSU Joint Department of Biomedical Engineering
University of North Carolina at Chapel Hill
Chapel Hill, NC 27599, USA

Z. Zhang
Department of Computer Science and Engineering
Michigan State University
East Lansing, MI 48824, USA

K. Huang
Chapel Hill High School
Chapel Hill, NC 27516, USA

DOI: 10.1002/adfm.202507821

patient, in leverage with artificial intelligence to make them more practical and efficient in daily healthcare management.[3–5] For instance, in patients recovering from neuromuscular disorders, effective rehabilitation requires both sensory feedback and physical stimulation. A system that integrates a strain sensor for joint movement and muscle contraction monitoring, a temperature sensor to track local inflammation, and stimulation electrodes for neuromuscular therapy can provide a synergistic approach, enhancing rehabilitation outcomes compared to isolated functional modules.[6–10] In wound healing applications, combining temperature and pH sensors enables monitoring of local inflammation and exudate pH to detect early signs of infection. Furthermore, electrical stimulators can be integrated to promote tissue regeneration through noninvasive intervention, enhancing the wound-healing process.[11–14] Patients with chronic kidney disease could benefit from creatinine, chloride, and pH sensors that monitor sweat biomarkers, offering a comprehensive assessment of kidney function and electrolyte balance.[15,16] These tailored combinations of modules enable the collection of highly relevant physiological data, facilitating more targeted interventions while optimizing resource utilization by including only necessary components. This synergistic effect can yield richer data and enhance the precision of health monitoring, leading to faster and more effective interventions. However, current wearable systems often lack the modularity and mechanical adaptability essential for personalized long-term healthcare applications.[17–19] Many multi-modal wearable platforms that attempt to integrate multiple sensors and actuators are bulky and inflexible, compromising comfort and practicality, especially for continuous wear.[20–22] Additionally, most systems are designed with fixed functionalities, limiting their scalability, replaceability, and adaptability to evolving healthcare needs, making it challenging to integrate or substitute functional modules over time without redesigning the entire platform.[23] Another challenge is the integration of diverse modules to allow structural continuity without sacrificing device footprint.[24] Furthermore, wearable devices are prone to unexpected damage such as scratches, pokes, rubs, and tears during daily use, which will affect their function in real-time on-body monitoring scenarios. Hence, personalized wearable systems require scalable modular reconfiguration and soft materials with skin-like mechanical properties, including self-healing capabilities and deformable properties, to ensure practical adaptability and reliability.

Self-healing bioelectronics presents a compelling solution for next-generation personalized wearable healthcare.[25,26] The self-healability of soft electronics can enable the fabrication of modular and reconfigurable electronics with self-repairable capability.[27,28] These types of electronics can achieve versatile customization and seamless integration of different modules by a simple mechanical cut and self-healing process. Self-repairable properties, like human skin, can enable devices to heal from unexpected damage and recover their mechanical and electrical properties. Unlike traditional modular assembly methods like adhesives or mechanical fasteners for constructing modular wearables, self-healing bioelectronics enables continuous, on-demand integration of diverse modules and ensures platform integrity via molecular-level restoration, resulting in a cohesive system rather than a loosely assembled device. Moreover, the self-healing properties eliminate additional assembly steps, autonomously maintaining stable connections. This enables rapid and efficient integration of new modules without extra support mechanisms, reducing both manufacturing complexity and costs. This open-interface approach makes the platform easily adaptable to new sensors or stimulators without the need to redesign the manufacturing platform. Additionally, flexibility as well as smooth and unified connections enabled by the soft self-healing materials enhance the comfort and aesthetic of the wearable devices, providing a more user-friendly experience. Recent advances in self-healing materials include self-healing elastomers, composites, hydrogels, and ion gels (summarized in Table S1, Supporting Information).[29] Self-healing elastomers provide high stretchability and durability but often require conductive fillers to achieve electrical functionality. Composites integrate conductive phases for multifunctionality but suffer from fabrication complexity and limited interfacial healing.[30,31] Hydrogels offer biocompatibility and softness, yet their water-based nature leads to poor long-term stability and limited electrochemical performance.[32–34] In contrast, self-healing ion gels, composed of crosslinked polymer networks swollen with ionic liquids, stand out due to their mechanical softness and stretchability, high self-healing efficiency, electrochemical stability, and high ionic conductivity.[35] The dynamic interactions, such as hydrogen bonding or ion–dipole interactions,[24] enable them to autonomously heal after damage, while the ionic liquid phase ensures stable operation under diverse environmental conditions.[36] These properties make the self-healing gel ideal for flexible wearable electronics and energy storage devices.[37–39] However, existing systems are often limited to single-mode or dual-mode sensing and rarely support modular integration due to challenges in mechanical compliance, material compatibility, and reliable electrical reconnection after self-healing. Although they have been reported in soft actuators and energy storage fields,[40] their applications in modular and reconfigurable wearable systems remain unexplored, particularly as mechanically and electrically self-healable interfaces for connecting various functional modules. This would provide a more reliable and comfortable platform for personalized wearable healthcare.

In this work, we developed a self-healing bioelectronic system that offers highly personalized customization, excellent mechanical compatibility with skin, and effective self-repairability. This system utilizing a self-healing soft gel provides the flexibility to seamlessly assemble andintegrate various functional modules allowing both physiological monitoring and therapeutic interventions to be tailored for individual needs. The flexibility of gels ensures skin conformity and optimal comfort, while the self-healing ability enables the system to autonomously repair mechanical damage, maintaining sustained performance. Moreover, compositional modulation of gels with glycerol and ionic liquid enables fine-tuning of their softness, toughness, and ionic conductivity, allowing the properties of gels to be tailored to meet specific functional requirements of each module. By selecting and assembling the required modules from a library of functional components,

H. Wang
Department of Electrical and Computer Engineering
Duke University
Durham, NC 27708, USA

including strain sensors, temperature sensors, sweat-biomarker sensors like glucose, creatinine, and chloride sensors, electrical stimulators, heaters, and others, the on-skin platform can be customized potentially for a variety of health monitoring scenarios such as wound healing, neuromuscular rehabilitation and thermal stress in high-risk occupations. In the monitoring modules of sweat biomarkers, we strategically utilize a microporous bilayer structure to facilitate efficient sweat absorption and storage. The bilayer microporous design enhances sweat-handling capacity and breathability, ensuring comfort during skin wear and reliable biomarker monitoring. Additionally, the fabricated flexible and self-healable energy storage devices based on ion gels are expected to facilitate self-powered and closed-loop systems, further enhancing the functionality of personalized wearable platforms. The customizable modular bioelectronics based on self-healing gels developed here provides a flexible and resilient solution for creating wearable systems that adapt to the evolving healthcare needs of individual patients, laying a foundation for personalized healthcare technologies.

2. Results and Discussion

2.1. Personalized Wearables Based on Self-Healing Gels

Personalized wearable healthcare devices hold great promise as a user-centered solution to address clinical care tailored to individual users.[41,42] Unlike traditional one-size-fits-all approaches, the systems (**Figure 1**a) we developed feature modular flexibility that effectively leverages a self-healing gel as a substrate to minimize manufacturing complexity. Moreover, strategically combining multiple synergistic biosensors without excession enables the functionality of the system to exceed the sum of its individual components, thus offering augmented diagnostic precision and comprehension. The modularity here is facilitated by self-healing gel, in a form of puzzle pieces, containing various biosensors, as depicted in Figure 1b–d. Initially, these puzzle pieces are separate, each with distinct functionalities, such as strain sensors, temperature sensors, pH sensors, sweat biomarker sensors, electrical stimulators, and others (Figure 1b). Upon heating at 70 °C for 20 min, the assembled pieces (Figure 1c) chemically merge due to the self-healing properties of the gel, forming a cohesive system with consistent structural integrity and soft mechanics, as shown in Figure 1d. The personalized selection of modules allows effective accommodation for user-specific needs, ranging from neuromuscular rehabilitation via sensing strain and temperature and stimulating, wound healing via sensing temperature and pH and electrical stimulation, chronic kidney disease monitoring via sensing creatinine, chloride, and pH, and so on (Figure 1e). Figure 1f (left) presents optical images of 2D and 3D architectures constructed from reassembled self-healing gels, demonstrating their capability to accommodate heterogeneous modules, as indicated by the varied colors of the petals serving as individualized matrices for hosting various functionalities. Specifically, the modular sensors realized via patterning distinct functional nanomaterials such as poly(3,4-ethylenedioxythiophene) polystyrene sulfonate (PEDOT:PSS), gold, and MXene are integrated into gel-based petals (Figure 1f, right). After drop-casting the nanomaterial layer or transferring the gold membranes onto the gel substrate uniformly, a near-infrared (NIR) laser beam is used to pattern this coated layer through localized ablation, thereby creating embedded functional units without observable damage to the underlying gel. This approach can be generally applicable to a wide variety of soft materials and nanomaterials, enabling the formation of highly integrated systems incorporating various sensors and stimulators. The left images of Figure 1g and Figure S1 (Supporting Information) show representative combinations of discrete functionalized gel petals, allowing on-demand customization. Subsequently, these modular components are assembled and integrated after heating and self-healing (Figure 1g, right), demonstrating the ability of the modular design to flexibly combine and adjust specific functional units for user-specific customization. Moreover, the modules can be assembled in desired quantities and rearranged (replaced, added, or removed), enabled by their self-healing properties (Figure 1d,g). Puzzle pieces, hexagons, or squares are suitable component shapes for planar tiling systems.

2.2. The Self-Healing Mechanism, Mechanical Characterization, and Biocompatibility Assessment of the Gel

The self-healing ion gels used above were synthesized by one-step photopolymerization of a solution containing monomers (acrylic acid, AA, and acrylamide, AAm), ionic liquid (1-ethyl-3-methylimidazolium ethyl sulfate, EMIES) and/or glycerol, crosslinker (N,N′-methylenebis(acrylamide), MBAA) and photoinitiator (Irgacure 2959, I2959). We modulate the ionic conductivity and mechanical softness of the gel for various wearable modules by adjusting the relative composition of glycerol and ionic liquid. The gel's molecular structure is illustrated in **Figure 2**a. The ionic liquid EMIES coupling with poly(acrylic acid) and poly(acrylamide) chains forms a tough polymer network. Glycerol containing hydroxyl groups is uniformly distributed in the matrix of the ion gel via hydrogen bonding with carboxyl groups in AA and amide groups in AAm. The pristine ion gel (without glycerol) exhibits a relatively high modulus due to the presence of polymer-rich nanodomains that phase separate from the otherwise solvated gel.[40,43] Interestingly, when gradually replacing EMIES with glycerol (from 100 wt.% ionic liquid to 0 wt.%), the reduction in electrostatic interactions induced by ionic liquid leads to a decrease in the overall crosslinking density of the gel, making the polymer network structure less compact. Furthermore, hydroxyl groups in the glycerol molecules can form hydrogen bonds with polymer chains, which are weaker than electrostatic interactions, resulting in a gel structure that is more prone to breaking and reassembling. Therefore, this modification in the gel composition makes it softer, exhibiting a lower Young's modulus (35.65 kPa for 0 wt.% ionic liquid content) and a higher fracture strain with decreased tensile strength (≈1350%, 135.51 kPa, for the same sample) compared to previously reported ion gels,[40] which enhances its conformability when interfacing with skin (Young's modulus of human skin is 10–500 kPa),[44,45] as shown in Figure 2b. Figure S2 (Supporting Information) shows the gel can be stretched without rupture, and it can be stably attached to the skin surface, showcasing its suitability for wearable applications. Figure 2d–g demonstrates the stable stretchability of ion gels with different compositions. Figure 2d,e exhibits cyclic loading-unloading curves for

Figure 1. High-throughput personalized point-of-care system based on self-healable sensing modules. a) Conceptual illustration of personalized wearable platforms based on self-healable modular sensing units. b) Optical images of various self-healable sensing modules. The sensing modules use gels as supporting matrix and embed functional nanomaterials, including strain sensor, temperature sensor, pressure sensor, heater, electrical stimulator, pH sensor and biochemical sensor like glucose, chloride and creatinine sensor, to feature a broad range of sensing functionalities. c) An optical image of manually assembled sensing modules. d) An optical image of self-healed freestanding sensing modules integrated as a single entity. The gel supporting matrixes can heal into a single piece after being treated at 70 °C for 20 min. e) Envisioned utilities of self-healable modular sensors for high-throughput personalized point-of-care monitoring tailored to specific clinical needs, including neuromuscular rehabilitation, wound healing and chronic kidney disease monitoring. f) Left: Optical images of biomimetic architectures based on self-healing gels used in the sensing modules; Right: Schematic illustration of the hybrid integration of various distinct modular sensors via self-healing of the supporting matrix, featuring the capability in manufacturing heterogeneous sensors on a same supporting platform. g) Left: Optical images of distinct sensing modules in separate pieces; Right: Corresponding whole flowers standing on an artificial skin after self-healing integration, demonstrating the wearable personalization and customization. Scale bars, 1 cm.

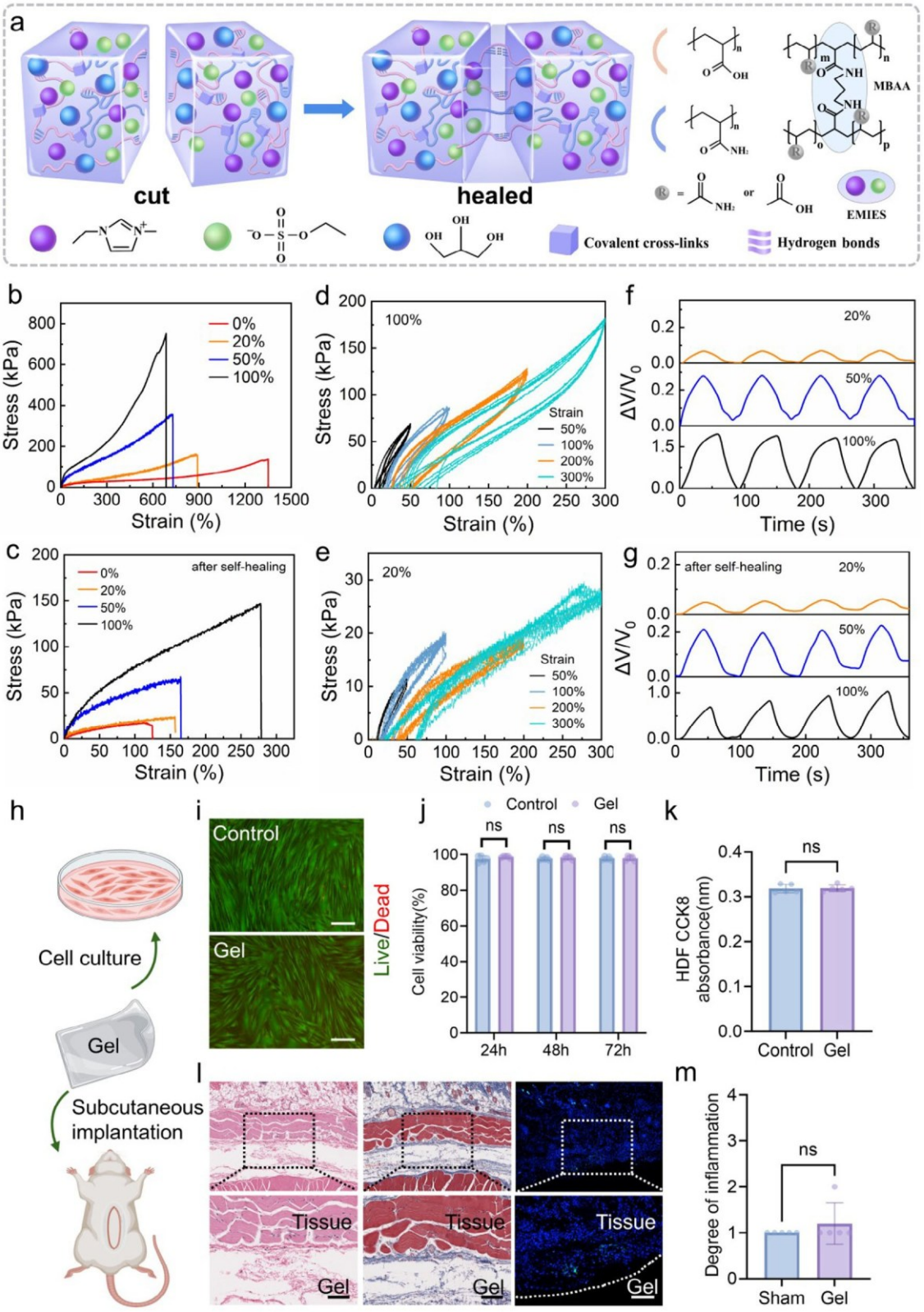

Figure 2. The self-healing mechanism, mechanical characterization, and in vitro and in vivo biocompatibility assessment of the gel. a) Schematic illustration showing self-healing mechanism and corresponding molecular structures of the gel. Measured tensile stress–strain curves of b) pristine and c) self-healed gels (70 °C, 20 min) with varying ionic liquid content. 0%, 20%, 50%, and 100% represent the weight content of ionic liquid relative to the total weight of ionic liquid and glycerol. The same applies to the following. Cyclic loading-unloading curves of ion gels containing d) 100 and e)

ion gels containing 100 and 20 wt.% ionic liquid, respectively, showcasing the stability of their mechanical properties under repeated stress. The gels with higher ionic liquid content demonstrate greater mechanical resilience, which is consistent with the fact that higher ionic liquid content maintains stronger electrostatic interactions and cross-linking, enhancing the structural robustness of the gels. The real-time relative voltage outputs of different ion gels under a maximum strain of 50% are shown in Figure 2f,g. The *y*-axis scale indicates that the addition of glycerol reduces the voltage output response due to its insulating properties. By adjusting the ratio of ionic liquid to glycerol, the electrical properties of the ion gels can be tuned as needed. After self-healing, this property can be mostly maintained.

The self-healing capability of the ion gel is crucial for realizing customization and maintaining the structural and functional integrity of the aforementioned modular system. Figure 2a illustrates the self-healing mechanism of the gel. The carboxyl groups in AA and amide groups in AAm form numerous reversible hydrogen bonds, allowing the polymer chains to rearrange and restore their original structure after damage. EMIES provides ionic conductivity and reduces interactions between polymer chains, facilitating their movement and rearrangement during damage, thereby promoting the self-healing process. Additionally, MBAA serves as a crosslinker to provide covalent cross-linking points and maintain the integrity of the network. Upon substitution of EMIES with glycerol, although the overall polymer network becomes looser, the reduction in ionic liquid diminishes the local mobility and flowability of the chains, and the high viscosity of glycerol and increased hydrogen bonds further restrict the free movement and rearrangement of the chains. This means that during the self-healing process, the efficiency of local chain reorganization decreases, making the process slower. In a word, while glycerol increases the overall deformability and softness of the gel, its high viscosity and increased hydrogen bonds hinder local chain mobility, thereby reducing the efficiency of self-healing (Figure 2c), which reflects a delicate balance between macroscopic softness and local chain reconfiguration ability. The relevant mechanical property parameters before and after self-healing and healing efficiencies are summarized in Tables S2 and S3 (Supporting Information) and a more detailed description is shown in Note S1 (Supporting Information). Although the mechanical performance of the gel after self-healing is slightly inferior to the original gel, it can provide sufficient freestanding stability and remain stable at strain levels well above those in daily wearable applications (with a fracture strain of 125–275% across gel compositions), as shown in Figure 2b,c.[32] Figure S3 (Supporting Information) shows the mechanical performance of the 0 wt.% gel sample over repeated cut-heal cycles. After ten consecutive cut-heal cycles (70 °C for 20 min), the stress–strain curves remained largely consistent, with the fracture strain and stress retaining 94% and 78% of their initial values, respectively. These results indicate that the connections formed through the self-healed interface maintain good mechanical stability and structural integrity even after multiple cut-heal cycles. The mechanism here is fundamental for the realization of modular soft bioelectronics. It also provides the required softness and adaptability for comfortable skin interfacing and maintains the robustness needed for long-term application.

To evaluate the biocompatibility of the gel (0% ionic liquid and 100% glycerol), we performed co-culture of human dermal fibroblast (HDF) cells with the gel and subcutaneous implantation of the gel in a rat (Figure 2h). Detailed procedures appear in the Experimental Section. Live/dead staining of HDF cells after 48 h of incubation with and without the gel reveals high cell viability in both groups, as indicated by abundant green fluorescence (live) and minimal red fluorescence (dead), suggesting no observable cytotoxicity induced by the gel (Figure 2i). Quantitative analysis of cell viability at 24, 48, and 72 h demonstrates no statistically significant difference between the gel-treated and control groups (Figure 2j), further confirmed by the cell counting kit-8 assay (Figure 2k), indicating excellent cytocompatibility of the gel. To assess the tissue response in vivo, the gel was subcutaneously implanted in rats for 7 days, followed by histological and immunological evaluation. Hematoxylin and eosin staining shows intact tissue morphology and minimal infiltration of inflammatory cells (Figure 2l, left), while Masson's trichrome staining reveals mild collagen deposition and thin fibrotic encapsulation surrounding the gel (Figure 2l, middle). Moreover, immunofluorescence staining for the cluster of differentiation 68 indicates a low level of macrophage infiltration at the implantation area (Figure 2l, right), suggesting a mild immune response. The histological assessment confirms these observations, showing very mild inflammation in both gel-implanted and control groups (Figure 2m), thus demonstrating a good in vivo biocompatibility of the gel. Overall, the gel exhibited desirable biocompatibility, as illustrated by minimal cytotoxicity in vitro, low inflammation in vivo, and thin fibrotic tissue formation, indicating its adequate biosafety for use in wearable systems and its potential for implantable bioelectronics.

2.3. Versatile Physiological Sensing and Stimulation Modules Based on Self-Healing Gels Integrated with Functional Nanomaterials

To realize a wide variety of wearable functions in physiological sensing, sweat sensing, electrotherapy, and thermal heating, we present a generalizable approach that allows the

20 wt.% ionic liquid, illustrating the stability of the stress response. The real-time relative voltage output of f) pristine and g) self-healed ion gels (70 °C, 20 min) with different ionic liquid content, under cyclic strains alternating between 0% and 50%. h) Schematic illustration of cell culture with the gel and subcutaneous implantation of the gel in rat. i) Representative live/dead stained images of human dermal fibroblasts (HDF) cells cultured with and without the gel for 48 h. Live cells were stained green and dead cells red. Scale bar: 200 µm. j) Quantitative analysis of HDF cell viability after co-culture with the gel and control groups for 24, 48, and 72 h. k) Cell counting kit-8 analysis of HDF cells after 48 h culture with and without the gel. l) Microscopy images of the surrounding tissues with hematoxylin and eosin staining indicating fewer inflammatory cells (left), Masson's trichrome staining indicating less fibrotic tissue thickness (middle), and immunofluorescence staining for cluster of differentiation 68 suggesting a mild immune response (right) in the implanted gel group after 7 days. Scale bar: 200 µm. m) Degree of inflammation evaluated by a blinded pathologist (0, normal; 1, very mild; 3, severe; 4, very severe). Bar height, mean; error bars, s.d.; $n = 5$ independent samples. ns indicates no statistically significant difference.

functionalization of various nanomaterials on the self-healing gel with feature resolution up to 100 μm, as illustrated in **Figure 3**. First, self-healing gel substrates in the target shape, petal-shaped here, were prepared via a one-step photopolymerization method. Functional nanomaterials, including MXene, PEDOT:PSS, and gold, were then drop-cast/transferred onto gel substrates. Next, the functional materials were patterned as required for specific module functions using a NIR laser beam. Benefiting from the solution processability of the gel precursor, we can fabricate substrates of diverse shapes and sizes based on device or assembly requirements and achieve rapid assembly through self-healing properties. The prepared substrates are compatible with various materials and can withstand NIR laser exposure, thereby offering material versatility. These modules—temperature sensors, heaters, strain sensors, pressure sensors, pH sensors, and electrical stimulation electrodes—can function independently or be combined as part of a modular system for comprehensive monitoring and targeted therapy. Figure 3a presents a schematic of an MXene-based temperature sensing module (thickness, 3 μm; serpentine width, ≈200 μm) on the self-healable gel. Figure 3b demonstrates the sensing stability of the temperature sensor over multiple thermal fluctuation cycles, with a consistent temporal correlation observed between the relative resistance change and temperature. The calibration curve in Figure 3c exhibits an ideal linear regression, indicating a reliable temperature sensitivity of 2.87‰ $°C^{-1}$. The performance of this MXene-based temperature sensor can be further enhanced to better meet clinical requirements through MXene surface functionalization or integration with high-precision amplification circuits.[46] Figure 3d displays an infrared thermograph of the MXene-based serpentine heater (thickness, 3 μm; serpentine width, ≈400 μm), which demonstrates its localized thermal effect through a uniform heat distribution and highlights its potential as a temperature-regulating component. The insert provides a schematic view of the heater. Figure S4 (Supporting Information) further indicates the efficacy of the heater, characterized by its fast thermal response (with temperature increasing from 25 to 45 °C in 180 s. And the heating response can be further enhanced by reducing the thickness of MXene film). Figure 3e illustrates the measured calibration curve of a strain sensor made of gold (thickness, 200 nm; serpentine width, ≈200 μm), depicting a highly linear correlation between strain and resistive sensing signal, demonstrating its suitability for precise strain monitoring in the range of 0–15%. A pH sensor based on pH-sensitive hydrogels which are composed of PEDOT and poly(vinyl alcohol) (PVA) is shown in Figure 3f. The calibration curve of this sensor shows a reliable linear relationship between resistive change and pH, with a sensitivity of 4.15% pH^{-1}, covering a broad range from acidic (pH ≈4) to basic (pH ≈9) environment. The schematic illustrates the pH-sensitive hydrogel component (dark blue rectangular blocks, Note S2, Supporting Information) and the electrical connection through gold electrodes to transmit resistance changes. Based on the piezoresistive effect and ionic conductivity of the ion gel,[47] we fabricated a pressure sensor, as shown in Figure 3g, where the ion gel serves as the ionic conductor anchored onto gold interdigital electrodes on a polyimide substrate. The ion gel consists of hydrogen-bonded domains connected by highly solvated and soft domains, forming a tough and stretchable structure that enables stable and uniform dispersing of pressure. Pressure-induced deformation can alter ion distribution and mobility within the ion gel, ultimately changing its electrical properties.[48] Figure 3h,i demonstrate a consistent relationship between applied pressure and relatively resistive changes, with a pressure sensitivity of 0.09% kPa^{-1}, indicating reliable performance across repetitive loading and unloading cycles. Figure S5 (Supporting Information) further details the performance of the ion gel-based pressure sensor under varying ionic liquid contents. These results indicate that ion gels with different compositions exhibit distinct pressure-sensing behaviors, which can provide a tuning window to adjust the sensor's properties for specific applications. As one of the therapeutic intervention modules, the MXene-based multichannel electrodes are shown in Figure 3j, consisting of a 3 × 3 electrode array and two reference electrodes. Figure 3k presents recorded segments of electrical stimulation, organized following the spatial arrangement of the electrode array. Each channel exhibits synchronized and conformal output during the cycles of pulsed electrical stimulation, illustrating the system's capability to stimulate multiple regions simultaneously. Differences in signal intensities between channels highlight spatial variations in electrical propagation. Figure 3l provides the corresponding instantaneous electrophysiological mapping recorded across the electrode array at a specific time point marked by the vertical line in Figure 3k, capturing the spatiotemporal voltage distribution. This unit demonstrates the potential for precise and localized modulation of electrical activity, which is essential for therapeutic interventions such as wound healing and neuromuscular rehabilitation.[49] Figure S6 (Supporting Information) illustrates the strain distribution on a skin-interfaced heating gel patch during the uniaxial stretch (15%), obtained from finite element analysis (FEA) simulation. The simulation shows that a higher strain is concentrated at the skin-gel interface along the stretching direction, while the strain distribution within the gel remains relatively low. This demonstrates that the gel can effectively dissipate strain, reducing electrode deformation (≈4%) and enhancing skin comfort and mechanical stability for wearable devices. However, a notable strain concentration is observed at the gel-electrode interface, which can be attributed to mechanical mismatch between the gel and electrodes. This issue will be discussed in detail later. Overall, the modular components mentioned above (Figures 1 and 3) demonstrate the versatility of the self-healing gels functionalized with distinct nanomaterials. The adaptable designs enable their potential in providing comprehensive physiological sensing and feedback, which is crucial for the development of next-generation wearable healthcare devices tailored to individual needs.

2.4. Self-Healable Sensing Modules for Sweat Biomarkers

Sweat is a valuable biofluid for non-invasive health monitoring, containing various biomarkers that reflect physiological state.[50,51] To harness this potential, we developed modular colorimetric sensors embedded in a microporous matrix within self-healing gels to detect key biomarkers such as glucose, creatinine, chloride, and pH levels in sweat (**Figure 4**a). Figure 4b shows a schematic illustration of the sweat colorimetric sensing modules. The microporous foam (FlexFoam) incorporated with colorimetric reagent serves as a detection reservoir and is embedded in hexagonal self-healable gels. The darker blue

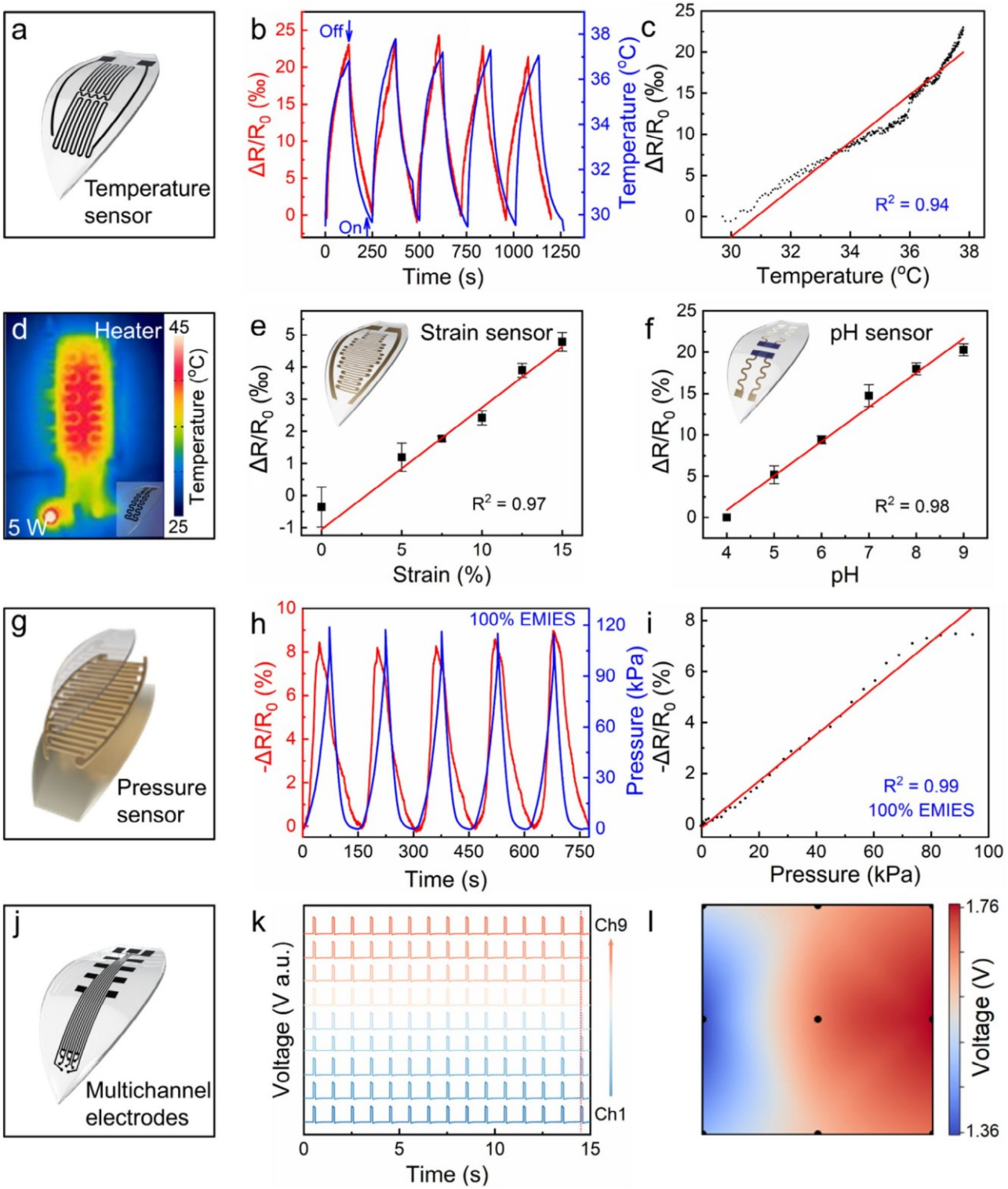

Figure 3. Characterization of self-healable functional modules for various physiological sensing and stimulation. a) Schematic view of a temperature sensor based on printed MXene electrodes. b) Measured temporal correlation between relative output resistance and temperature of MXene-based temperature sensor (R_0 = 615.67 Ω) and c) the calibration curve as a function of temperature. The negative values of $\Delta R/R_0$ at the beginning could be attributed to minor instrumental disturbances or noise during measurement. d) Infrared thermograph of a MXene-based heater showing its thermal effects. Insert: schematic view of the heater. e) Calibration curve of an Au-based strain sensor under various strains (R_0 = 242.86 Ω). The negative values of $\Delta R/R_0$ at the beginning could be attributed to minor instrumental disturbances or noise during measurement. Each point, mean; error bars, standard deviation (s.d.); n = 3 independent samples. Insert: schematic view of the strain sensor. f) Measured correlation between output resistance and environmental pH of a PEDOT:PSS/PVA hydrogel based pH sensor (R_0 = 2.48 MΩ). Each point, mean; error bars, s.d.; n = 3 independent samples.

regions at the bottom of the microporous foam represent the state of sweat absorption, with orange spheres indicating the colorimetric indicators that responded to targeted analytes in sweat. The light blue part with pale yellow spheres indicates a standby state waiting for the arrival of sweat to initiate biochemical sensing. The microporous foam is a polymeric foam made of polyacrylate foam and polypropylene, exhibiting superior sweat absorption capacity and breathability due to its bilayer microporous structure compared with conventional filter paper. Scanning electron microscopy (SEM) images and corresponding size distribution histograms in Figure 4b and Figure S7 (Supporting Information) provide a comprehensive analysis of the microporous structure, suggesting the presence of two distinct layers (Note S3, Supporting Information). The lower layer with larger pores can absorb liquid quickly upon contact and keep the skin surface dry and comfortable. The denser upper layer can disperse and store a significant amount of liquid, maintaining high absorption capacity and structural integrity. Video S1 (Supporting Information) shows the absorption behavior of the bilayer microporous foam when it absorbs different volumes of liquid and absorbs a large amount of liquid continuously. The capillary action and adsorption effect of the microporous structure provide the driving force for anti-gravity water absorption.[52] Notably, during the absorption process, the microporous foam expands only in the vertical direction (limited to the low-porosity layer) without any lateral expansion behavior. When at most 5 μL of water is absorbed, the high-porosity layer is where most water is stored at, while past 5 μL, liquid is vertically transferred to and primarily stored in the low-porosity layer. Using the section of Video S1 (Supporting Information) demonstrating the absorption of 20 μL of water in ≈6 s as a basis, we extracted the fluxes at which water entered and the diffusion properties for each microporous layer. We validated the diffusion properties by implementing them into a FEA simulation of the rapid sorption of 20 μL of water, as shown in Figure 4c and Figure S8a–d (Supporting Information). The results show that as more liquid is absorbed, the low-porosity layer gradually expands to accommodate more storage, while the high-porosity layer, once saturated, only transports liquid without further absorption or expansion. At saturation point, more than 60% of the total liquid is stored in the upper layer, despite its smaller initial volume. Overall, this model corroborates the experimental data regarding the instant flux of water. Figure S8 and Note S4 (Supporting Information) provide details of the simulation. Having validated the FEA model for the sorption-swelling behavior of the microporous foam, we then moved on to create a predictive model for the sorption under sweat conditions. Figure 4d and Figure S8e–h (Supporting Information) present simulation results at a sweat rate of 0.02 μL mm^{-2} min^{-1} for the sorption of 20 μL of sweat. Due to the low liquid flux relative to the diffusion coefficient, there is no significant difference in the liquid molar concentration within layers. Like Figure 4c and Figure S8a–d (Supporting Information), Figure 4d and Figure S8e–h (Supporting Information) also demonstrate that water is primarily stored in the low porosity layer once the high porosity layer reaches saturation. Overall, this design facilitates efficient sweat absorption and storage, ensuring reliable biomarker detection while maintaining user comfort. The microporous foam seamlessly connects to the surrounding gel, with a small amount of gel diffusing into the porous network acting as an adhesive, ensuring robust device integrity (Figure 4a). Figure S9 (Supporting Information) shows the tensile stress–strain curves of the microporous foam embedded in gel compared to its standalone counterpart. The increase of fracture strain and strength observed in the embedded sample indicates that the gel provides extra mechanical reinforcement and ensures a secure connection with the foam. This solid integration enhances the durability and robustness of the sensing module in practical applications.

The quantitative analysis of glucose i), creatinine ii), and chloride iii) concentrations as well as pH values via UV–vis absorption spectra (top) and corresponding optical images (bottom) captured under consistent lighting conditions are shown in Figure 4e,g and Figure S10 (Supporting Information). The quantitative sensing mechanism for these biomarkers in sweat is based on colorimetric sensing. The principles by which chemical indicators react with various molecular biomarkers and produce color changes are detailed in Note S5 (Supporting Information). The observed colorimetric changes indicate a clear concentration-dependent variation in absorbance. The calibration curves for each biomarker in Figure 4f demonstrate a strong linear correlation between absorbance at specific wavelengths and biomarker concentrations. The calculated sensitivities for glucose, creatinine, and chloride are 0.024% a.u. μm^{-1}, 0.32% a.u. μm^{-1} and 0.87% a.u. mm^{-1}, respectively. Glucose concentration in sweat (0.01–0.3 mm) is far lower than in plasma, and our current module operates near the upper edge of this range. That means it can diagnose hyperglycemia but unable to resolve small fluctuations.[53] Replacing the I^-/I_2 chromogenic pair with higher-extinction dyes or plasmonic readouts, together with faster glucose-oxidase variants or peroxidase-mimetic nanozymes, should amplify the optical signal and lower the limit of detection for full sweat-level coverage.[54] Creatinine is an important marker for monitoring hydration status and renal function.[55] Normal sweat creatinine levels typically range from 20 to 130 μM, but elevated levels may indicate dehydration or impaired kidney function.[56] The sensor here covers a relevant range for detecting such abnormalities. Chloride concentration in sweat is a crucial marker for cystic fibrosis and

Insert: schematic view of the pH sensor. The dark blue rectangular blocks represent pH-sensitive PEDOT:PSS/PVA hydrogel and its resistance changes under different pH conditions can be transmitted by the Au electrodes. g) Illustration of an exploded view of a pressure sensor comprising ion gel as ionic conductor, Au interdigital electrodes as metallic conductor and polyimide substrate from top to bottom. Pressure induces deformation of ion gel, affecting the distribution and mobility of ions within, which ultimately alters electrical properties of the ion gel. h) Temporal response of relative output resistance in the ion gel-based pressure sensor during repetitive cycles of loading and unloading (R_0 = 3.04 MΩ). i) Measured resistive change of the pressure sensor in response to applied pressure. j) Schematic view of MXene-based multichannel electrodes for electrical stimulation. There is a 3 × 3 electrode array and two reference electrodes. k) Segments of the recorded electrical stimulation and the data are displayed following the spatial arrangement of the electrode array. l) Instantaneous electrophysiology mapping recorded across the 3 × 3 MXene-based electrode array. The timing of the voltage map is indicated in k) by the vertical line.

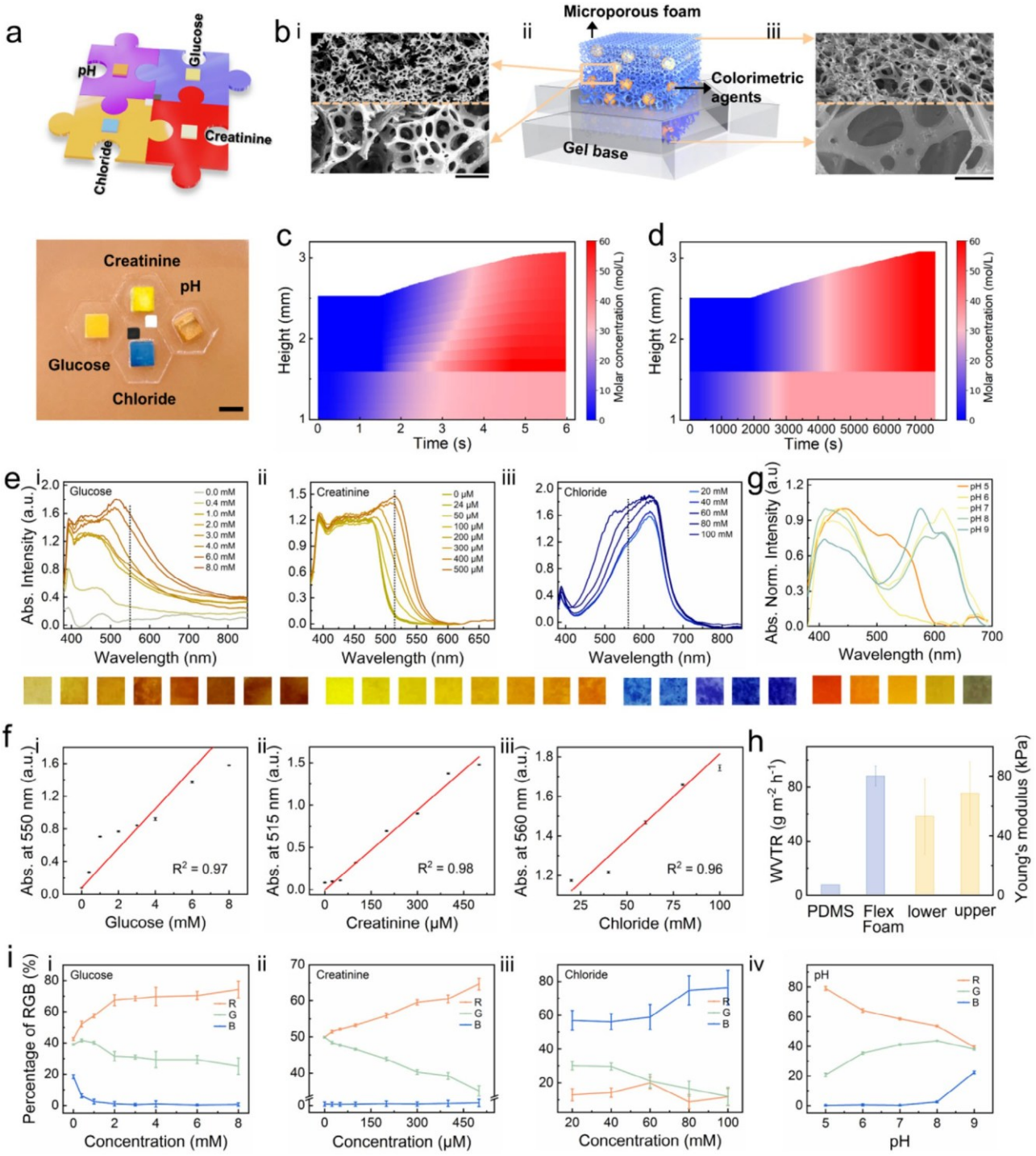

Figure 4. Self-healable sensing modules for quantitative colorimetric analysis of biomarkers in sweat. a) A schematic illustration (top) and an optical image (bottom) of self-healable sweat sensors, featuring colorimetric detection reservoirs based on microporous matrix embedded with various colorimetric reagents for determining concentrations of glucose, creatinine and chloride, and pH values in sweat. The black and white blocks are reference color markers. Scale bar, 3 mm. b) (i) Scanning electron microscope (SEM) images of cross-sections of the sweat-wicking material, microporous foam, featuring its high porosity (lower) and low porosity (upper) layers. (ii) A schematic illustration of a sweat sensing module featuring the bilayer microporous foam embedded in hexagonal gel. The lower dark blue microporous foam represents the state after absorbing sweat, with orange spheres indicating a colorimetric reaction between indicators and biomarkers in sweat. The upper light blue part represents microporous foam not yet in contact with sweat, with pale yellow spheres that have not undergone a color change. (iii) SEM images corresponding to bottom and top surfaces of the microporous foam, respectively. Scale bars, (i) 20 µm, (iii) 10 µm. Mapping of liquid molar concentration and changes in the thickness of the microporous foam over time c) under simulated experimental conditions with a sufficient liquid source at one end of high-porosity layer for the sorption of 20 µL of water in 6 s and d) at real sweat rates (0.02 µL mm^{-2} min^{-1}) for the sorption of 20 µL of water. The initial thickness of the high-porosity layer is 1.6 mm, and that of the

electrolyte balance.[57] The sensing module covers a relatively wide concentration range from 20 to 100 mm, with a detection limit sufficient to differentiate between normal levels and those indicative of cystic fibrosis (above 60 mm). The sensor's colorimetric response across a range of pH values, which is essential for evaluating hydration and metabolic health, is shown in Figure 4g. The pH of sweat typically ranges from 5.0 to 7.0 and deviations from this range can signal issues with hydration or metabolic imbalance.[58] Interference testing for glucose, creatinine, and chloride detection is provided in Figure S11 and Note S5 (Supporting Information), demonstrating that the colorimetric sensors maintain reliable performance despite the presence of other sweat biomarkers. Figure 4h presents the water vapor transmission rate of polydimethylsiloxane (PDMS) and the microporous foam, further demonstrating the high breathability of the microporous foam, which can facilitate skin perspiration and improve biocompatibility.[59] The high-porosity bottom layer, with a lower Young's modulus (54.51 kPa) compared to the top layer (70.11 kPa), better matches the modulus of human skin, creating a softer, more comfortable interface. This increased softness can be attributed to the multiscale microporous foam. Additionally, the FEA simulation in Figure S12 (Supporting Information) illustrates the strain distribution on the skin-interfaced sweat-sensing gel patch under uniaxial stretch (15%). The results demonstrate that the gel effectively disperses strain and provides a buffering layer to minimize the deformation of the center-embedded microporous foam (≈2%). Since the sensors here can capture the physiologically relevant ranges with visible shifts in color, it enables convenient on-body measurement, as information can be visually extracted from the color. Figure 4i provides calibration curves that quantify the relationships between %RGB values from colored microporous blocks in Figure 4e,g and concentrations of glucose i), creatinine ii) and chloride iii) and pH values iv), demonstrating the sensor's capability to track and quantify biomarker concentrations based on color changes. The microporous foam used here is designed for single-use sensing, as the chromogenic reactions and visual outputs are irreversible. During short-term on-body tests (as shown later in Figure 6), no reagent leaching or signal drift was observed, indicating good chemical stability. To enhance its long-term reliability, strategies such as microencapsulation of reagents[60] and antifouling surface modifications (e.g., hydrophilic or zwitterionic coatings,[61] peelable porous polytetrafluoroethylene films)[62] could prevent degradation and contamination and further enhance device durability. Potential reuse may be achieved by reloading chromogenic reagents after cleaning the used microporous foam. This scheme offers a simple and intuitive method for in situ measurement of biomarker concentrations during and immediately after sweat collection using an effective microporous foam instead of extensive microfluidic channels for sweat collection. Although the detection limit and sensitivity of biomarker monitoring are currently constrained by the selected detection reagents, this modular design provides a universal and simple strategy for personalized sweat biomarker tracking.

2.5. Self-Healable and Flexible Zinc-Air Batteries for Wearable Energy Storage

With the increasing demand for flexible, durable, and efficient energy storage solutions in wearable electronics and biointegrated systems, zinc-air batteries stand out due to their high energy density, environmental friendliness, and cost-effectiveness.[63,64] However, the integration of zinc-air batteries into flexible and wearable devices presents challenges, particularly in maintaining performance under mechanical deformation and long-term use. Here, we present a flexible and self-healable zinc-air battery based on the ion-gel solid electrolyte, which can withstand significant mechanical stress with negligible impact on performance. Even after breakage, it can restore functionality through the self-healing mechanism illustrated in Figure 2a. Also, the ion gel as a solid electrolyte can eliminate the risk of electrolyte leakage and enhance structural stability, which will improve the overall longevity and safety of the battery. These make the ion gel-based solid electrolyte a promising strategy for flexible and reliable energy storage systems in wearable electronics. **Figure 5a** provides a schematic view of the zinc-air battery, including an exploded view of each layer. The zinc foil serves as the anode where zinc undergoes oxidation, releasing electrons and generating zinc ions (Note S6, Supporting Information). The porous carbon and manganese oxide (MnO_2) serve as the cathode, where the porous carbon provides a large surface area for the oxygen reduction reaction and MnO_2 acts as a catalyst. A steel grid supports the cathode structure. Between two electrodes, the ion gel solid electrolyte ensures continuous ion transport. The bottom-left and top-right images in Figure 5a show that the prepared zinc-air battery has comparable planar dimensions to a commercial zinc-air button battery (AMZ13-60ZM) while being much thinner. A single zinc-air battery exhibits a stable open circuit voltage (OCV) of ≈1.0 V under ambient conditions (Figure 5b; Figure S13a, Supporting Information). Figure 5c,d shows the OCVs over a week of zinc-air batteries bent at 90° and 180° continuously. Compared to flat state, the bent batteries exhibit similar and stable OCVs, demonstrating their good flexibility and mechanical durability. It is noted that the OCV of the assembled battery after mechanical cutting and subsequent self-healing remains at the same level as the pristine sample, indicating that the self-healing capability of the ion gel solid electrolyte can help maintain battery performance (Figure 5e). Furthermore, when an electrode

low-porosity layer is 1 mm. e) Quantitative colorimetric analysis of the concentrations of (i) glucose, (ii) creatinine and (iii) chloride by UV–vis absorption spectroscopy (top) and optical images (bottom). The dashed lines mark the wavelengths selected for quantitative analysis in the corresponding calibration curves. f) Corresponding calibration curves at various concentrations of (i) glucose, (ii) creatinine and (iii) chloride. Each point, mean; error bars, s.d.; n = 3 independent samples. g) The normalized UV–vis absorption spectra (top) and optical images (bottom) of samples at different pH values. h) Water vapour transmission rate (left) of PDMS and microporous foam, illustrating the superior breathability of the microporous foam, and Young's modulus (right) of the upper and lower layers of the microporous foam, indicating the better softness of the upper layer that touches the skin. Bar height, mean; error bars, s.d.; n = 6 independent samples. i) Standard calibration curves between normalized %RGB values and concentrations of (i) glucose, (ii) creatinine, (iii) chloride and (iv) pH values. Each point indicates the average value of all pixels in the colored microporous foam block at the bottom of e) and g); error bars, s.d.; n = 3 independent samples.

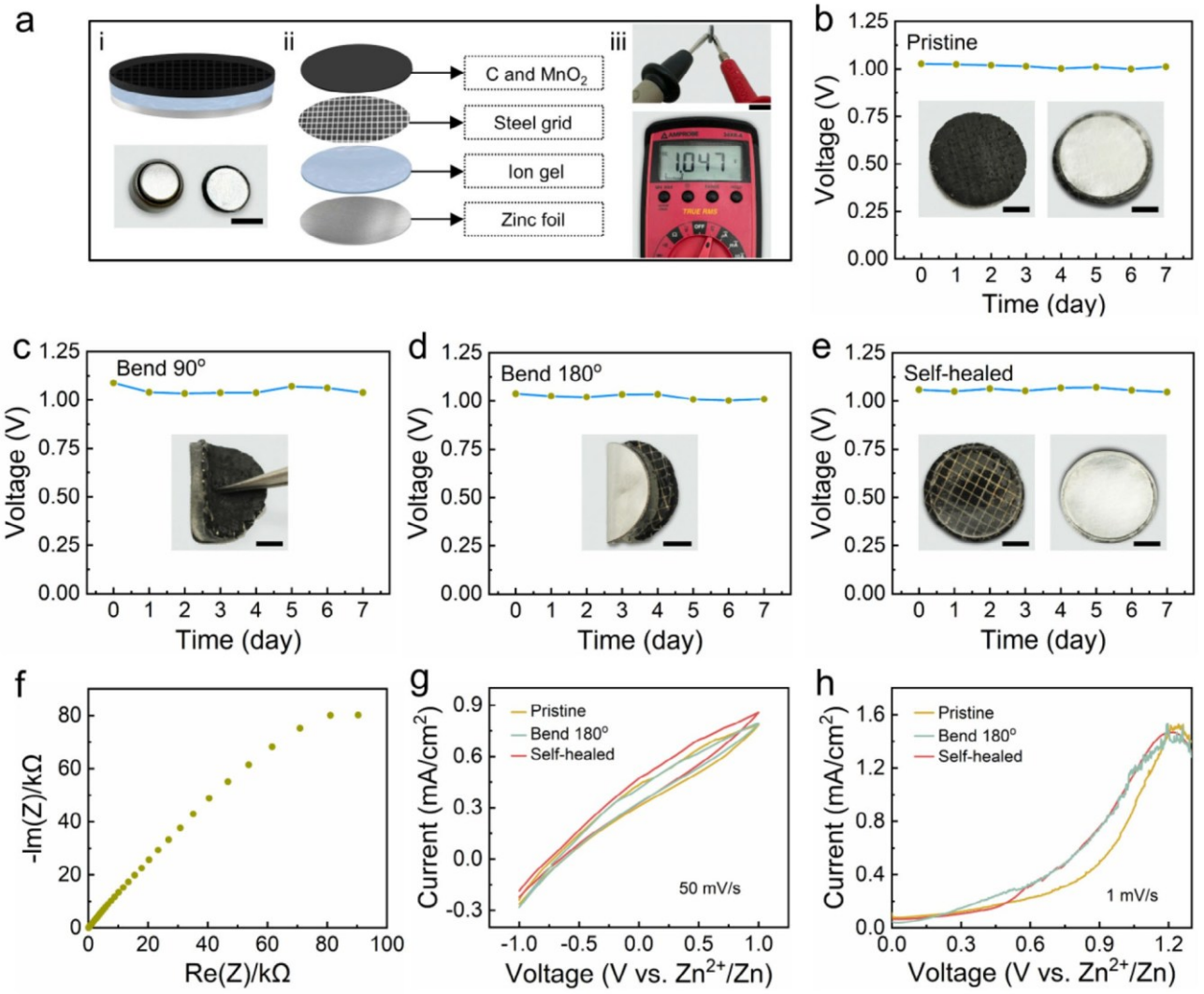

Figure 5. Self-healable and flexible zinc-air batteries based on ion gel solid electrolytes. a) (i) A schematic view of the self-healing ionogel-based zinc-air battery (top) and an optical image of the commercial zinc-air button battery (model number: AMZ13-60ZM; bottom left) and the fabricated ionogel-based zinc-air battery (bottom right). Scale bar, 5 mm. (ii) Illustration of an exploded view of the ionogel-based battery. (iii) Photographs showing the open circuit voltage (OCV) of an as-prepared zinc-air battery measured using a multimeter. Scale bar, 1 cm. OCVs of as-prepared ionogel-based zinc-air batteries over a week under b) pristine state, c) continuously bent at 90°, d) continuously bent at 180° and e) after self-healing, demonstrating the stability of output voltage under various deformations. Scale bars, 2 mm. f) Electrochemical impedance spectroscopy (EIS, Nyquist plot) of the ion gel solid electrolyte. g) Cyclic voltammetry (CV) curves at a scan rate of 50 mV s^{-1} and h) Linear sweep voltammetry (LSV) curves at a scan rate of 1 mV s^{-1} for pristine, 180° bent, and self-healed ionogel-based zinc-air batteries.

is damaged or the anode is depleted, the electrode can be easily replaced, allowing for self-healing induced reassembly (inset of Figure 5e). Chronopotentiometric analysis (Figure S13b,c, Supporting Information) further confirms the stable and sustained discharge behavior of the battery under constant current conditions, and the energy density is calculated to be 2.77 Wh kg^{-1}. The ionic conductivity of the ion gel solid electrolyte is investigated via electrochemical impedance spectroscopy (EIS) measurements with two stainless steel blocking electrodes. It is calculated to be 2.88×10^{-3} S cm^{-1} based on the bulk resistance in Figure 5f, indicating an efficient ion transport for electrochemical reactions.[65] After fracture healing, the ionic conductivity of the ion gel is 2.52×10^{-3} S cm^{-1} (Figure S14a, Supporting Information), maintaining 87.50% of the original value. Figure S14b (Supporting Information) complements a frequency-dependent analysis of the impedance. The impedance decreases with increasing frequency, showing resistive behavior at high frequencies, which corresponds to the low bulk resistance in Figure 5f. At lower frequencies, the phase angle decreases to −60°, showing capacitive behavior due to charge accumulation and redistribution within the electrolyte. The electrochemical performance of pristine, 180° bent, and self-healed ionogel-based zinc-air batteries is demonstrated via cyclic voltammetry (CV) and linear sweep voltammetry (LSV) curves in Figure 5g,h. Figure 5g shows a smooth and continuous transition from negative to positive current as the voltage sweeps between −1 and 1 V, demonstrating

typical redox behavior of zinc oxidation at the anode and oxygen reduction at the cathode. All samples exhibit nearly overlapping profiles including consistent peak current values, reflecting stable electrochemical activity across different battery states. This suggests that the ion gel solid electrolyte can sustain effective ion transport and charge transfer and electrode reactions can continue to occur in all states, even under deformation or after mechanical damage and repair, ensuring consistent battery operation. The LSV curves at a scan rate of 1 mV s^{-1} further assess the oxygen reduction reaction activity of the ionogel-based battery in different states (Figure 5h). The smooth rise in current as the voltage increases across all conditions, with similar peak currents, further validates the robust performance of the battery, demonstrating unaffected reaction kinetics and consistent capacity. The limiting current density suggests that the rate of oxygen diffusion controls the overall reaction rate and future optimization of the electrode structure or electrolyte composition could potentially improve the limiting current density and enhance the overall performance of the battery. The demonstrated performance of the battery here suggests promising potential for integrating self-healable energy sources into personalized wearable bioelectronic platforms to enhance energy autonomy.

2.6. On-Body Demonstration of the Self-Healable Personalized Wearable Sensing System

To further demonstrate the functionality of the wearable sensing modules and the personalized biosensing platforms mentioned above in practical applications, **Figures 6** and S15 (Supporting Information) present representative monitoring for tracking physiological and metabolic changes during various physical activities and metabolic states. Figure 6a,b display the relative resistance changes of a strain sensing module mentioned in Figure 3e in response to different body motions when placed on various body parts. One is placed on the wrist and can continuously monitor compression and stretching during wrist movements, as shown in Figure 6a. The starting position is set with the fist and forearm held horizontally. When the wrist bends downward, the sensor is compressed, causing a decrease in resistance, which increases upon returning to the initial position. Conversely, bending the wrist upward stretches the sensor, leading to an increase in resistance. The right part shows the sensing signal variation between the lower and upper bending limits. Similarly, Figure 6b depicts a strain sensor attached to the inner elbow, tracking forearm movements as the arm is raised and lowered. The starting position is set with the arm hanging vertically. The blue line represents the signal variation as the forearm bends upward at ≈90°. The orange line shows the change when the forearm is bent upward to its limit. Both illustrate the sensor's ability to provide real-time mechanical feedback from different joints, which is crucial for movement analysis during rehabilitation or physical activity monitoring. A temperature sensing module shown in Figure S15a,b (Supporting Information) is used to monitor forehead temperature variations during and after cycling, as depicted in Figure 6c, showcasing its potential for assessing the onset of fever, heat stress, or other metabolic imbalances. To demonstrate the potential of the colorimetric sensing modules for sweat monitoring as shown in Figure 4, we conducted a two-day study monitoring sweat biomarkers in two subjects. A general timeline of the study is displayed in Figure 6d. Concentrations of various chemicals and pH values in sweat were recorded in the fasting state, 1 h after eating, 1 h after drinking, and during cycling exercise (Figure S15c, Supporting Information). For subject 1 in Figure 6e, the pH of sweat remained stable after eating, increased to 7 following water intake, typically due to dilution from hydration, and decreased to 5.5 during cycling as a result of acidic metabolic byproducts from physical activity. The creatinine concentration increased after eating due to metabolic activity, decreased after drinking, and showed moderate levels during cycling. For subject 2 in Figure 6f, the chloride concentration increased after eating, decreased following water intake, and remained elevated during cycling, reflecting the effects of salt intake, fluid dilution, and increased excretion. The glucose concentration remained constant but dropped to zero during cycling (In reality, glucose levels would not drop to absolute zero. This observed value reflects the detection limit of the glucose sensor discussed above. The value indicates a decrease in glucose concentration in sweat after exercise.), likely due to increased glucose utilization. This study illustrates the potential of wearable sweat sensing modules for monitoring hydration levels, electrolyte balance, and metabolic responses to food and physical activity. Figure 6g and Figure S15d (Supporting Information) display the mechanical adaptability of the wearable platform, which responds to and accommodates dynamic deformations such as skin compression and stretching. This flexibility of gels ensures consistent and stable contact with the skin. Figure 6h–k and Figure S15e–h (Supporting Information) show the FEA simulation results of the strain distribution on skin-interfaced sensing gel patches under 15% uniaxial stretch (The stretching process is shown in Video S2, Supporting Information.). The simulation demonstrates that the wearable patches can effectively conform to skin deformation, with the gel layers exhibiting lower strain levels (6–13%) than the surrounding skin, indicating their role in dissipating stress and buffering deformation to protect the sensing parts. While the gel reduces the overall deformation in the sensors (≈4% for electrodes and ≈2% for the microporous foam), the gel-sensor interfaces still exhibit relatively high strain due to the mechanical mismatch between gels and sensors (≈25% for the gel-electrode interface and ≈18% for the gel-microporous foam interface). This indicates that enhancing the interface design (such as incorporating a flexible transition layer, using more flexible electrode materials, and optimizing the geometry)could further improve the mechanical stability and durability of the wearable systems. The wearable patch can be comfortably worn on different body parts (bottom of Figure 6l). The physiological data monitored using various customized biosensing platforms after activities such as cycling or squatting are demonstrated in Figure 6l,m. The mobile application interface shown in Figure 6n demonstrates how the data from tailored wearable biosensing platforms can be processed and visualized, enabling users to track their physiological metrics conveniently on their smartphones and providing a personalized health monitoring experience.

3. Conclusion

In this study, we developed a customizable modular soft bioelectronic system based on self-healing gels. This platform supports

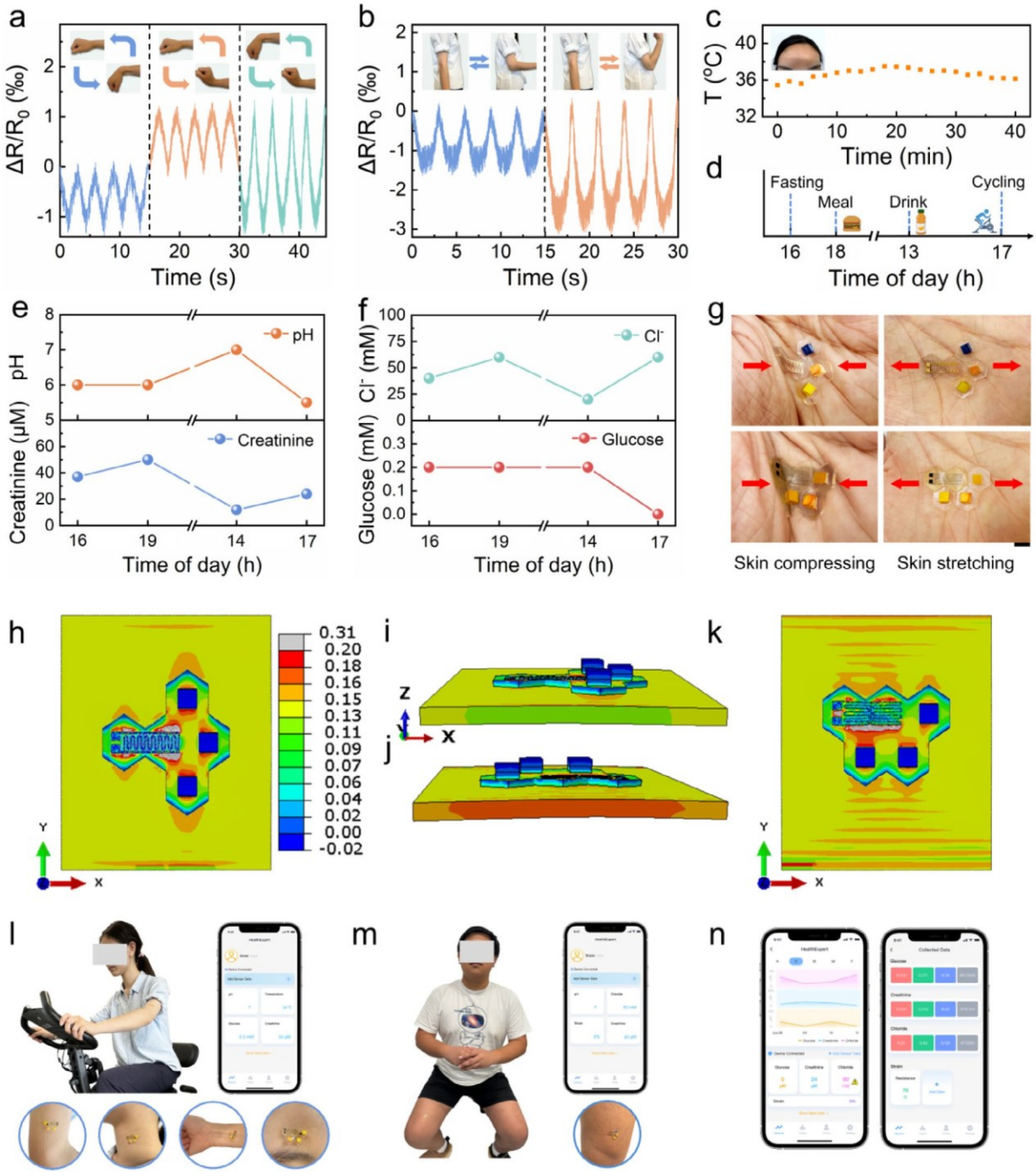

Figure 6. On-body demonstration of the personalized wearable system toward physiological and metabolic monitoring. a) A strain sensor placed on the wrist, monitoring continuous compression downward and stretching upward at various angles. b) A strain sensor attached to the elbow, monitoring repeated raising and lowering of the forearm at various angles. c) A temperature sensor used to monitor forehead temperature variations while cycling (first 20 min) and at rest (last 20 min). d) Timeline for a 2-day subject study. For the cycling activity, cycle for 25 min, take a 10-min break, and then cycle for another 25 min. Temporal changes of e) pH values and concentrations of creatinine and f) concentrations of chloride and glucose in sweat. Collect sweat 1 h after eating and drinking. g) Representative device combinations on human skin, demonstrating flexibility and mechanical reliability under skin compressing and stretching. Scale bars, 5 mm. Finite element analysis (FEA) simulation results showing the distribution of strain in the h,k) X-Y plane and i,j) X-Z plane of representative skin-interfaced gel patches under 15% uniaxial stretch applied in the Y direction. The rectangle represents the stretched skin and the hexagon represents the gel. The serpentine pattern and square represent the physiological sensor and sweat sensor (embedded the microporous foam with colorimetric reagent), respectively. l) Photographs of a heathy volunteer wearing the tailored sensor patch during cycling exercise (upper left) and at different body parts (bottom), with a photo showing information obtained from the upper arm picture (upper right). m) A photograph of another heathy volunteer wearing the tailored sensor patch during squatting exercise (left) and a close-up of the patch on the thigh with a photo showing information (right). n) Enhanced custom mobile application designed for physiological sensing and metabolic tracking.

a simple yet effective integration of various sensor and stimulator modules, offering mechanical compliance and system reconfigurability. The modular nature of this system allows for any assembly of various functional components, such as strain sensors, temperature sensors, and biochemical sensors for glucose, creatinine, and chloride monitoring. This flexibility enables the platform to be tailored to specific healthcare needs. For instance, the integration of temperature sensors with pH sensors can provide a comprehensive assessment of wound healing processes, while chloride and creatinine sensors are critical for monitoring chronic kidney disease and metabolic disorders. Moreover, compositional modulation of the gel allows for tuning its ionic conductivity and mechanical properties including softness and toughness, based on the device requirements. The biomarker monitoring modules leverage a bilayer microporous foam for efficient sweat absorption, ensuring breathability and comfort for extended skin contact. Additionally, we developed flexible and self-healable zinc-air batteries based on ion gels to support on-skin bioelectronic platforms, which hold promise for creating self-powered and closed-loop wearable systems. The self-healing gel-based modular bioelectronic platform developed here offers a customizable and versatile solution for personalized health monitoring. While the platform supports the sensing of physical and biochemical signals within physiologically relevant ranges, there are still some limitations. For example, the colorimetric glucose sensor used here exhibits a higher detection limit compared to enzymatic electrochemical sensors, limiting sensitivity at low concentrations. Future improvements could involve replacing the I^-/I_2 chromogenic pair with higher-extinction dyes or plasmonic readouts and enhancing the enzymatic system using glucose-oxidase variants or peroxidase-mimicking nanozymes to improve signal strength and lower the limit of detection. Additional efforts in optimizing self-healing efficiency, electrode-gel interface stability, and system-level integration with flexible energy storage units will further enhance the utility of this platform, paving the way for more adaptive and resilient bioelectronic systems tailored to individual clinical needs.

4. Experimental Section

Materials: Acrylamide (AAm, 99%), Acrylic acid (AA, 99%), N,N'-methylenebis(acrylamide) (MBAA, 99%), 1-ethyl-3-methylimidazolium ethyl sulfate (EMIES, 95%), Glycerol (99.5%), 2-hydroxy-4′-(2 hydroxyethoxy)-2-methylpropiophenone (I2959, 98%), poly(3,4-ethylene dioxythiophene) poly(styrene sulfonate) (PEDOT:PSS), poly(vinyl alcohol) (PVA, 99%), glucose oxidase from Aspergillus niger, peroxidase from horseradish, trehalose, potassium iodide (99.0%), chloride assay kit, pH indicator solution, L-ascorbic acid (LAA, 99.0%), sodium L-lactate (SLL, 98%), urea (analytical standard), potassium bromide (KBr, 99.0%), and sodium nitrate ($NaNO_3$, 99.0%), phosphate buffered saline (PBS) were purchased from Sigma–Aldrich. Sodium citrate buffer solution (pH 6.0) was purchased from Thermo Fisher Scientific. The creatinine assay kit was purchased from Creative BioMart. The microporous foam (FlexFoam) was purchased from Always. Kapton (polyimide) film (type HN) was purchased from CS Hyde Company. Gold leaf was purchased from SloFoodGroup. All the above chemicals were used directly without any further purification. Ultrathin MXene ($Ti_3C_2T_x$) flakes, ordered from Feynman Nano Co., Ltd, were utilized in a chemical exfoliation technique to produce a 10 mg mL^{-1} MXene dispersion in deionized water. Specifically, the MXene flakes were synthesized via the minimally invasive layer delamination method using LiF/HCl to generate in situ HF. The etching solution was prepared by mixing 9 m HCl with LiF before gradually adding Ti_3AlC_2 powder. After 48 h of etching at 35 °C, the products were washed with deionized water until pH >6. The sediment underwent ice-water bath sonication for 2 h to achieve single-layer $Ti_3C_2T_x$, followed by centrifugation to remove unexfoliated material. The resultant $Ti_3C_2T_x$ nanosheet solution was stored at 4 °C to prevent oxidation.[66]

Synthesis of Self-Healing Gels: Self-healing copolymer gels were synthesized using a one-step method via copolymerization of AAm and AA monomers. In a typical procedure, two monomers AAm (1.5975 g) and AA (0.5825 g) were dissolved in EMIES and/or glycerol (The total weight of EMIES and glycerol is 4.0672 g.), followed by sonication to obtain a homogeneous solution. Then, the covalent cross-linker MBAA (0.0046 g) and photoinitiator I2959 (0.0034 g) were added. The obtained solution was sonicated again under dark conditions for 30 min and subsequently poured into various designed molds and irradiated under ultraviolet light for 180 s at 175 mW cm^{-2} to obtain the copolymer gels.

Mechanical Measurements: The stress–strain curves of gels with different compositions were obtained with a tensile strength tester (Mark-10 ESM303) under continuous application of tensile strain. A baseline DC potential of 5 V, provided by a PowerLab system (16/35, ADInstruments Inc.), was applied to the gel, with additional circuits for power management and signal conversion from capacitance to voltage. The adhesion force between microporous foams and gels was also measured using the Instron machine (Mark-10 ESM303). For the self-healing test, the gel sample was cut into half pieces, and then pressed the cut surfaces of the two half pieces together, which were healed at 70 °C for 20 min. The healing efficiency can be improved by elevating temperature or prolonging time. The mechanical performance of self-healed samples was quantified by measuring the tensile stress–strain curves of the healed samples at 70 °C under 20 min on the same tester.

In Vitro Cytocompatibility Studies of the Gel: Primary human dermal fibroblasts (PCS-201-012, ATCC) were cultured in DMEM supplemented with 10% fetal bovine serum and 1% penicillin-streptomycin. Cells were maintained in a humidified incubator at 37 °C with 5% CO_2. For biocompatibility assessment, cells were seeded in contact with the gel, and viability was examined at 24, 48, and 72 h using the Live/Dead Cell Imaging Kit (R37601, Thermo Fisher). Live cells emitted green fluorescence (Ex/Em: 488/515 nm), and dead cells emitted red fluorescence (Ex/Em: 570/602 nm). Images were acquired using a fluorescence microscope with GFP and Texas Red filter sets. To assess cytotoxicity, a CCK-8 assay (CK04-01, Dojindo) was conducted after 48 h of incubation. After adding 10 µL of reagent to each well containing 100 µL of medium, plates were incubated at 37 °C for 2 h. Absorbance at 450 nm was measured using a microplate reader. Cell viability was determined by comparing absorbance values to the untreated control group.

In Vivo Biocompatibility Assessment of the Gel: Biocompatibility and histological analyses were conducted following protocols adapted from previously published methods.[67] Male Wistar rats (250–300 g, Charles River Laboratories, Boston, MA) were anesthetized using 2% isoflurane delivered by inhalation. Once fully anesthetized, a 1 cm incision was made along the dorsal side, and subcutaneous pockets were formed using blunt dissection. Test gels were placed into the pockets, and the wounds were closed with 4–0 polypropylene sutures (n = 5 per group). After seven days, the animals were euthanized, and tissue samples containing the gels and surrounding tissue were harvested. The inflammatory response at the implant site was examined through histological staining, including H&E, Masson's trichrome, and immunofluorescent labeling of CD68 with DAPI nuclear counterstain. A mouse monoclonal anti-CD68 antibody (MA5-13324, Thermo Fisher) was used, followed by a goat anti-mouse IgG (H+L) secondary antibody conjugated to Alexa Fluor 488 (Abcam). All procedures involving animals were approved by the Institutional Animal Care and Use Committee (IACUC) of Columbia University (Protocol no. AC-AABY0652) and carried out in accordance with institutional ethical guidelines.

Fabrication of Sensing Modules for Physiological Monitoring: The gel substrates were cured in an ultraviolet chamber by placing the precursor solution in a petal-shaped mold. The MXene solution and PEDOT:PSS solution were dropped cast onto the gel and heated at 40 °C for

drying. The gold leaf was pressed onto the substrate. After that, the functional materials were patterned with an infrared laser cutter (SFX-50GS). For the preparation of the pH-sensitive PEDOT:PSS/PVA hydrogel placed between the gold electrodes on the pH sensor, a 10 wt.% PVA solution was made by dissolving PVA powder in deionized water. Next, 5 wt.% PEDOT:PSS aqueous dispersion was added into the PVA solution, followed by slow mixing for 24 h. The prepared PEDOT:PSS/PVA solution was then poured into a glass spacer, followed by three cycles of freezing at −20 °C for 8 h and thawing at 25 °C for 3 h. The fabrication of pressure sensing modules was different from the others. A gold nanomembrane (Au, thickness ≈200 nm) and an adhesive chromium layer (Cr, thickness ≈10 nm) were deposited on a polyimide film (thickness ≈10 µm) via a metal sputtering (Kurt Lesker PVD 75). Au interdigital electrodes on the polyimide were formed using the laser cutting machine. Then, pressure-sensitive petal-shaped ion gel was placed on top of the electrodes to complete the circuit.

Characterization of Sensing Modules for Physiological Monitoring: The relative resistance changes in sensing modules were measured by a DMM. For measurement of pH sensitivity, the PEDOT:PSS/PVA hydrogels were submerged into a phosphate-buffered saline (PBS) solution with different pH values ranging from 4 to 9. In 5 min, hydrogels were removed from the PBS solution and their resistance was measured with DMM. Temperature mapping of the MXene-based heater during thermal ablation at an input power of 5 W was captured by an infrared camera (FLIR ONE Pro, FLIR Systems). Voltage was applied in situ for electrical stimulation using a DC 2 V power supply (PowerLab).

Characterization of the Sweat-Wicking Microporous Foam: The SEM images of the microporous foam were captured by the field emission scanning electron microscope (Hitachi S-4700). The WVTR test was performed on a C360M water vapor transmission rate test system at 23 °C, 90% RH. Young's modulus was measured using Optics11 Piuma Nanoindenter.

Sweat Absorption Simulation in the Microporous Foam: The simulation was performed using the commercial software package Marc Mentat from Hexagon software. The FEA model itself was a 2D shell made up of square elements. Appropriate material properties and fluxes were applied to each layer. The results obtained from the FEA simulations of the microporous foam sorption-swelling properties included changes in liquid concentration at representative points over time, changes in vertical displacement at representative points over time, and the thickness and liquid concentration of the microporous foam at different time increments during an FEA run. These measurements were taken for the microporous foam samples under instantaneous flux conditions and sweating conditions. Changes in concentration and displacement at representative points were measured at selected sample points on the FEA model, where data relating to changes in sample point position and concentration was extracted and graphed as functions of time. The concentration distribution and thickness of the microporous foam at different time intervals were measured with contour centroid plots on an FEA microporous foam model, with bands of different thicknesses representing the liquid concentration of a region of the microporous foam. For details, see Figure S16 and Note S4 (Supporting Information).

Quantitative Colorimetric Analysis of Biomarkers in Sweat: For the colorimetric analysis of glucose, creatinine, chloride, and pH, specific chromogenic reagents were prepared. For glucose detection, a mixture of glucose oxidase (1.2 mg), horseradish peroxidase (0.12 mg), trehalose (102 mg), and potassium iodide (99.6 mg) were dissolved in 1 mL of sodium citrate buffer solution (pH 6.0) to create the glucose detection cocktail. For creatinine detection, an alkaline picrate solution was prepared using 2 mL of creatinine sodium borate, 6 mL of creatinine surfactant, 10 mL of creatinine color reagent, and 3.6 mL of creatinine NaOH, which can react with creatinine for colorimetric detection. For chloride detection, a chloride assay kit was used, and a universal pH indicator solution served as the chromogen for pH detection. The microporous foam was immersed in these reagents, allowed to dry, and then embedded in the test zone at the center of hollow hexagonal gels. A small amount of gel solution was applied as an adhesive to bond and secure the microporous foam to the gel. The absorption spectra were recorded by a Vernier Go Direct SpectroVis Plus Spectrophotometer.

Electrochemical Characterization: The electrochemical properties were investigated by a Biologic SP-50e system. The electrolyte was sandwiched between two stainless steel electrodes for conductivity measurements and the electrical conductivity was tested via EIS over the frequency range of 0.1 Hz to 1 MHz. The ion gel was sandwiched between zinc foils and carbon electrodes to form cells. CV measurements were performed at a scan rate of 50 mV s^{-1} in the voltage range of −1 to 1 V, with the zinc foil serving as the working electrode and the carbon electrode as the counter electrode. The LSV curves, measured at a scan rate of 1 mV s^{-1}, used the same electrode configuration as in the CV tests. All measurements were conducted in ambient conditions.

On-Body System Validation: All procedures were conducted in accordance with the National Institutes of Health Guide and with the approval of the Office of Human Research Ethics at the University of North Carolina at Chapel Hill, under protocol no. 22–0163. Informed consent was obtained from all participants before enrollment. Testing involved five healthy adults (aged 20–30) as volunteers. All subjects provided their consent prior to participation. The strain sensor was placed on the wrist or inner elbow of the subjects. Subjects performed wrist flexion or arm lifting movements in a lab at 25 °C. The signals were recorded continuously during the movements. The temperature sensor was affixed to the subject's forehead while she performed moderate-intensity cycling at 25 °C and 60% RH. The cycling activity lasted for 20 min, followed by a 20-min rest, with signal recorded every 2 min throughout the test. In the biomarker concentration monitoring, relevant sensing modules were attached to the chest of two subjects. Sweat was induced either through a shower (water temperature: 38–42 °C, ≈10 min) followed by staying in the shower room for ≈15 min or through natural sweating during cycling. The dimension of the microporous foam reservoir used was 2.8 × 2.8 × 2.6 mm, with a saturation absorption volume of 20 µL. Once saturated, photos were taken using an iPhone 15 Pro, and the RGB values were extracted to determine the creatinine concentration and pH value in the sweat of subject 1 at fasting, 1 h after eating, 1 h after drinking, and during cycling. For subject 2, the glucose and chloride concentrations in sweat were monitored under the same conditions. Representative bioelectronic platforms composed of different sensing modules were placed on the upper arm of a female subject or the thigh of a male subject to monitor relevant physiological parameters during moderate-intensity cycling or squatting exercises. The tests were conducted at 25 °C and 60% RH.

FEA Simulation of the Strain Distribution on Skin-Interfaced Sensing Gel Patches: FEA simulations were conducted using the commercial software Abaqus to analyze the strain distribution on various skin-interfaced sensing gel patches under uniaxial stretching. The models consisted of a 35 × 35 × 2 mm skin substrate, hexagonal gel patches, and surface-integrated/embedded sensors (serpentine and square geometries). The simulations employed 3D solid elements (C3D8R) for the skin, gel, and microporous foam, and shell elements (S4R) for the electrodes. A total of 47953 nodes and 36645 elements were used, with refined meshing at the gel-sensor interfaces to accurately capture localized strain. Displacement-controlled boundary conditions were applied to simulate uniaxial stretch of 15% in either the X or Y directions. The explicit dynamic solver was used to capture the deformation response over a total simulation time of 1 s. The material parameters used in the simulations are provided in Table S4 (Supporting Information).

Statistical Analysis: No data points were excluded as outliers. All quantitative data are reported as mean ± standard deviation (s.d.). The number of independent samples (n) for each dataset is indicated in figure legends (typically n = 3–6). No formal hypothesis testing or group comparisons were conducted for this study. As this work focuses on device-level proof-of-concept demonstrations, no additional statistical adjustments (e.g., post-hoc tests or alpha corrections) were applied. For calibration curves and sensor performance metrics, linear regression was performed using Origin to extract sensitivity and correlation coefficients (R^2). The pore sizes of microporous foams were analyzed using Image J. RGB values of the biomarker sensor images were extracted using MATLAB. For cell viability and histological analysis, unpaired two-tailed Student's t-tests were used to compare the two groups. A p-value less than 0.05 was considered statistically significant. Analyses were performed using GraphPad Prism 9

(GraphPad Software, CA). Non-significant differences are marked as "ns" in the figures.

Supporting Information

Supporting Information is available from the Wiley Online Library or from the author.

Acknowledgements

This work was supported by the fund from the National Science Foundation (award # ECCS-2139659) and the National Institute of Biomedical Imaging and Bioengineering at the National Institutes of Health under award number 1R01EB034332-01. This work was performed in part at the Chapel Hill Analytical and Nanofabrication Laboratory, CHANL, a member of the North Carolina Research Triangle Nanotechnology Network, RTNN, which is supported by the National Science Foundation, Grant ECCS-2025064, as part of the National Nanotechnology Coordinated Infrastructure, NNCI.

Conflict of Interest

The authors declare no conflict of interest.

Author Contributions

A.Z., Z.Y., and B.G. contributed equally to this work. A.Z. and W.B. conceived the ideas and designed the research. A.Z., Z.Y., Y.W., Y.L., Y.S., E.T., S.X., B.D., G.Y., W.X., and Y.W. fabricated and characterized the samples. B.G. and B.M. performed the simulation. A.Z., Z.Y., B.G., Y.C., K.L., Z.Z., and A.P. performed the data analysis. A.Z., Z.Y., B.G., K.H., H.W., B.M., K.C., and W.B. wrote the manuscript with input from all authors.

Data Availability Statement

The data that support the findings of this study are available from the corresponding authors upon reasonable request.

Keywords

modular bioelectronics, personalized medicine, self-healing ion gels, wearable sensors

Received: March 27, 2025
Revised: June 10, 2025
Published online:

[1] N. J. Schork, *Nature* **2015**, *520*, 609.
[2] L. H. Goetz, N. J. Schork, *Fertil. Steril.* **2018**, *109*, 952.
[3] J. Min, J. Tu, C. Xu, H. Lukas, S. Shin, Y. Yang, S. A. Solomon, D. Mukasa, W. Gao, *Chem. Rev.* **2023**, *123*, 5049.
[4] J. Kim, A. S. Campbell, B. E. F. de Ávila, J. Wang, *Nat. Biotechnol.* **2019**, *37*, 389.
[5] X. Mei, J. Li, Z. Wang, D. Zhu, K. Huang, S. Hu, K. D. Popowski, K. Cheng, *Nat. Mater.* **2023**, *22*, 903.
[6] M. Maddocks, C. M. Nolan, W. D. Man, M. I. Polkey, N. Hart, W. Gao, G. F. Rafferty, J. Moxham, I. J. Higginson, *Lancet Respir. Med.* **2016**, *4*, 27.
[7] Y. Liu, L. Tian, M. S. Raj, M. Cotton, Y. Ma, S. Ma, B. McGrane, A. V. Pendharkar, N. Dahaleh, L. Olson, H. Luan, O. Block, B. Suleski, Y. Zhou, C. Jayaraman, T. Koski, A. J. Aranyosi, J. A. Wright, A. Jayaraman, Y. Huang, R. Ghaffari, M. Kliot, J. A. Rogers, *NPJ Digit. Med.* **2018**, *1*, 19.
[8] A. Crema, M. Bassolino, E. Guanziroli, M. Colombo, O. Blanke, A. Serino, S. Micera, F. Molteni, *Med* **2022**, *3*, 58.
[9] D. Shen, K. Cheng, E. Marbán, *J. Cell. Mol. Med.* **2012**, *16*, 2112.
[10] S. Wang, Z. Zhang, B. Yang, X. Zhang, H. Shang, L. Jiang, H. Liu, J. Zhang, P. Hu, *Chem. Eng. J.* **2023**, *457*, 141136.
[11] J. W. Song, H. Ryu, W. Bai, Z. Xie, A. Vázquez-Guardado, K. Nandoliya, R. Avila, G. Lee, Z. Song, J. Kim, M.-K. Lee, Y. Liu, M. Kim, H. Wang, Y. Wu, H.-J. Yoon, S. Soo Kwak, J. Shin, K. Kwon, W. Lu, X. Chen, Y. Huang, G. A. Ameer, J. A. Rogers, *Sci. Adv.* **2023**, *9*, ade4687.
[12] S. Zhang, D. Zhu, X. Mei, Z. Li, J. Li, M. Xie, H. J. W. Lutz, S. Wang, K. Cheng, *Bioact. Mater.* **2021**, *6*, 1957.
[13] P. Mostafalu, A. Tamayol, R. Rahimi, M. Ochoa, A. Khalilpour, G. Kiaee, I. K. Yazdi, S. Bagherifard, M. R. Dokmeci, B. Ziaie, S. R. Sonkusale, A. Khademhosseini, *Small* **2018**, *14*, 1703509.
[14] Q. Pang, D. Lou, S. Li, G. Wang, B. Qiao, S. Dong, L. Ma, C. Gao, Z. Wu, *Adv. Sci.* **2020**, *7*, 1902673.
[15] Y. Yang, W. Gao, *Chem. Soc. Rev.* **2019**, *48*, 1465.
[16] S. Han, S. Yamamoto, C. Y. Jung, D. Y. Jin, T. Lee, J. S. Kim, *Commun. Mater.* **2024**, *5*, 153.
[17] J. R. Walter, S. Xu, J. A. Rogers, *Nat. Commun.* **2024**, *15*, 123.
[18] L. Wei, Z. Li, Z. Dai, L. Ding, H. Wei, J. Li, H. Zhu, Y. Zhu, *Adv. Mater. Technol.* **2024**, *9*, 2301812.
[19] N. Li, J. Peng, W. J. Ong, T. Ma, Arramel, P. Z., J. Jiang, X. Yuan, C. Zhang, *Matter* **2021**, *4*, 377.
[20] S. Hozumi, S. Honda, T. Arie, S. Akita, K. Takei, *ACS Sens.* **2021**, *6*, 1918.
[21] S. Wang, F. Gao, Y. Hu, S. Zhang, H. Shang, C. Ge, B. Tan, X. Zhang, J. Zhang, P. Hu, *Chem. Eng. J.* **2022**, *443*, 136446.
[22] S. Wang, X. Fan, Z. Zhang, Z. Su, Y. Ding, H. Yang, X. Zhang, J. Wang, J. Zhang, P. Hu, *ACS Nano* **2024**, *18*, 17175.
[23] K. Mahato, T. Saha, S. Ding, S. S. Sandhu, A. Y. Chang, J. Wang, *Nat. Electron.* **2024**, *7*, 735.
[24] J. Kang, J. B. H. Tok, Z. Bao, *Nat. Electron.* **2019**, *2*, 144.
[25] D. Son, J. Kang, O. Vardoulis, Y. Kim, N. Matsuhisa, J. Y. Oh, J. W. To, J. Mun, T. Katsumata, Y. Liu, A. F. McGuire, M. Krason, F. Molina-Lopez, J. Ham, U. Kraft, Y. Lee, Y. Yun, J. B. H. Tok, Z. Bao, *Nat. Nanotechnol.* **2018**, *13*, 1057.
[26] C. Liu, S. O. Kelley, Z. Wang, *Adv. Mater.* **2024**, *36*, 2401219.
[27] Y. Xia, Y. Zhu, X. Zhi, W. Guo, B. Yang, S. Zhang, M. Li, X. Wang, C. Pan, *Adv. Mater.* **2024**, *36*, 2308424.
[28] Z. Li, J. Lu, T. Ji, Y. Xue, L. Zhao, K. Zhao, B. Jia, B. Wang, J. Wang, S. Zhang, Z. Jiang, *Adv. Mater.* **2024**, *36*, 2306350.
[29] Y. Jiang, S. Ji, J. Sun, J. Huang, Y. Li, G. Zou, T. Salim, C. Wang, W. Li, H. Jin, J. Xu, S. Wang, T. Lei, X. Yan, W. Y. X. Peh, S. C. Yen, Z. Liu, M. Yu, H. Zhao, Z. Lu, G. Li, H. Gao, Z. Liu, Z. Bao, X. Chen, *Nature* **2023**, *614*, 456.
[30] J. Park, D. Seong, Y. J. Park, S. H. Park, H. Jung, Y. Kim, H. W. Baac, M. Shin, S. Lee, M. Lee, D. Son, *Nat. Commun.* **2022**, *13*, 5233.
[31] K. Cheng, D. Shen, J. Smith, G. Galang, B. Sun, J. Zhang, E. Marbán, *Biomaterials* **2012**, *33*, 2872.
[32] F. Mo, P. Zhou, S. Lin, J. Zhong, Y. Wang, *Adv. Healthcare Mater.* **2024**, *13*, 2401503.
[33] L. Luo, Y. Li, Z. Bao, D. Zhu, G. Chen, W. Li, Y. Xiao, Z. Wang, Y. Zhang, H. Liu, Y. Chen, Y. Liao, K. Cheng, Z. Li, *Adv. Mater.* **2024**, *36*, 2302686.
[34] H. Ren, W. Li, H. Li, Y. Ding, J. Li, Y. Feng, Z. Su, X. Zhang, L. Jiang, H. Liu, P. Hu, *Adv. Funct. Mater.* **2024**, *35*, 2417715.
[35] S. Wang, M. W. Urban, *Nat. Rev. Mater.* **2020**, *5*, 562.
[36] M. Wang, X. Xiao, S. Siddika, M. Shamsi, E. Frey, W. Qian, W. Bai, B. T. O'Connor, M. D. Dickey, *Nature* **2024**, *631*, 313.

[37] M. Qi, R. Yang, Z. Wang, Y. Liu, Q. Zhang, B. He, K. Li, Q. Yang, L. Wei, C. Pan, M. Chen, *Adv. Funct. Mater.* **2023**, *33*, 2214479.
[38] J. Kang, D. Son, O. Vardoulis, J. Mun, N. Matsuhisa, Y. Kim, J. Kim, J. B. H. Tok, Z. Bao, *Adv. Mater. Technol.* **2019**, *4*, 1800417.
[39] E. Palleau, S. Reece, S. C. Desai, M. E. Smith, M. D. Dickey, *Adv. Mater.* **2013**, *25*, 1589.
[40] M. Wang, P. Zhang, M. Shamsi, J. L. Thelen, W. Qian, V. K. Truong, J. Ma, J. Hu, M. D. Dickey, *Nat. Mater.* **2022**, *21*, 359.
[41] A. Libanori, G. Chen, X. Zhao, Y. Zhou, J. Chen, *Nat. Electron.* **2022**, *5*, 142.
[42] K. B. Johnson, W. Q. Wei, D. Weeraratne, M. E. Frisse, K. Misulis, K. Rhee, J. Zhao, J. L. Snowdon, *Clin. Transl. Sci.* **2021**, *14*, 86.
[43] S. Liu, Y. Wu, L. Jiang, W. Xie, B. Davis, M. Wang, L. Zhang, Y. Liu, S. Xing, M. D. Dickey, W. Bai, *ACS Appl. Mater. Interfaces* **2024**, *16*, 46538.
[44] T. Li, Y. Wang, S. Li, X. Liu, J. Sun, *Adv. Mater.* **2020**, *32*, 2002706.
[45] Y. Liu, M. Pharr, G. A. Salvatore, *ACS Nano* **2017**, *11*, 9614.
[46] M. Mozafari, M. Soroush, *Mater. Adv.* **2021**, *2*, 7277.
[47] Y. Wu, Y. Li, Y. Liu, D. Zhu, S. Xing, N. Lambert, H. Weisbecker, S. Liu, B. Davis, L. Zhang, M. Wang, G. Yuan, C. Z. You, A. Zhang, C. Duncan, W. Xie, Y. Wang, Y. Wang, S. Kanamurlapudi, G. G. Evert, A. Putcha, M. D. Dickey, K. Huang, W. Bai, *Sci. Adv.* **2024**,*10*, adp8866.
[48] S. R. A. Ruth, V. R. Feig, H. Tran, Z. Bao, *Adv. Funct. Mater.* **2020**, *30*, 2003491.
[49] D. Zhu, S. Liu, K. Huang, Z. Wang, S. Hu, J. Li, Z. Li, K. Cheng, *Circ. Res.* **2022**, *131*, 135.
[50] D. S. Yang, R. Ghaffari, J. A. Rogers, *Science* **2023**, *379*, 760.
[51] J. Chen, C. Zhou, P. Zheng, K. Cheng, H. Wang, J. Li, L. Zeng, P. Xie, *Behav. Brain Res.* **2017**, *332*, 280.
[52] A. Wysocki, H. Rieger, *Phys. Rev. Lett.* **2020**, *124*, 048001.
[53] H. Lee, C. Song, Y. S. Hong, M. Kim, H. R. Cho, T. Kang, K. Shin, S. H. Choi, T. Hyeon, D. H. Kim, *Sci. Adv.* **2017**, *3*, 1601314.
[54] I. Lee, D. Probst, D. Klonoff, K. Sode, *Biosens. Bioelectron.* **2021**, *181*, 113054.
[55] A. Koh, D. Kang, Y. Xue, S. Lee, R. M. Pielak, J. Kim, T. Hwang, S. Min, A. Banks, P. Bastien, M. C. Manco, L. Wang, K. R. Ammann, K.-I. Jang, P. Won, S. Han, R. Ghaffari, U. Paik, M. J. Slepian, G. Balooch, Y. Huang, J. A. Rogers, *Sci. Transl. Med.* **2016**, *8*, 366ra165.
[56] R. Cánovas, M. Cuartero, G. A. Crespo, *Biosens. Bioelectron.* **2019**, *130*, 110.
[57] J. Kim, S. Oh, D. S. Yang, L. Rugg, R. Mathur, S. S. Kwak, S. Yoo, S. Li, E. E. Kanatzidis, G. Lee, H. J. Yoon, Y. Huang, R. Ghaffari, S. A. McColley, J. A. Rogers, *Biosens. Bioelectron.* **2024**, *253*, 116166.
[58] S. Nakata, M. Shiomi, Y. Fujita, T. Arie, S. Akita, K. Takei, *Nat. Electron.* **2018**, *1*, 596.
[59] B. Zhang, J. Li, J. Zhou, L. Chow, G. Zhao, Y. Huang, Z. Ma, Q. Zhang, Y. Yang, C. K. Yiu, J. Li, F. Chun, X. Huang, Y. Gao, P. Wu, S. Jia, H. Li, D. Li, Y. Liu, K. Yao, R. Shi, Z. Chen, B. L. Khoo, W. Yang, F. Wang, Z. Zheng, Z. Wang, X. Yu, *Nature* **2024**, *628*, 84.
[60] X. Mei, L. Zhu, X. Peng, J. Yang, Y. Li, *Biomed. Anal.* **2024**, *1*, 64.
[61] S. Patel, F. Ershad, M. Zhao, R. R. Isseroff, B. Duan, Y. Zhou, Y. Wang, C. Yu, *Soft Sci.* **2022**, *2*, 9.
[62] Z. Song, R. Li, Z. Li, X. Luo, *Biosens. Bioelectron.* **2024**, *264*, 116640.
[63] S. Huang, F. Wan, S. Bi, J. Zhu, Z. Niu, J. Chen, *Angew. Chem., Int. Ed.* **2019**, *131*, 4357.
[64] H. Li, F. Xu, Y. Li, J. Sun, *Adv. Sci.* **2024**, *11*, 2402193.
[65] W. Liu, N. Liu, J. Sun, P. C. Hsu, Y. Li, H. W. Lee, Y. Cui, *Nano Lett.* **2015**, *15*, 2740.
[66] A. Thakur, N. B. S. Chandran, K. Davidson, A. Bedford, H. Fang, Y. Im, V. Kanduri, B. C. Wyatt, S. K. Nemani, V. Poliukhova, R. Kumar, Z. Fakhraai, B. Anasori, *Small Methods* **2023**, *7*, 2300030.
[67] A. Roy, S. Zenker, S. Jain, R. Afshari, Y. Oz, Y. Zheng, N. Annabi, *Adv. Mater.* **2024**, *36*, 2404225.